2D Materials

Ultrafast dynamics of bright and dark excitons in monolayer WSe_2 and heterobilayer WSe_2/MoS_2

To cite this article: Jan Philipp Bange *et al* 2023 *2D Mater.* **10** 035039

IOP Publishing 2D Mater. 10 (2023) 035039 https://doi.org/10.1088/2053-1583/ace067

2D Materials

OPEN ACCESS

RECEIVED
3 May 2023

REVISED
12 June 2023

ACCEPTED FOR PUBLICATION
21 June 2023

PUBLISHED
3 July 2023

PAPER

Ultrafast dynamics of bright and dark excitons in monolayer WSe_2 and heterobilayer WSe_2/MoS_2

Jan Philipp Bange[1], Paul Werner[1], David Schmitt[1], Wiebke Bennecke[1], Giuseppe Meneghini[2], AbdulAziz AlMutairi[3], Marco Merboldt[1], Kenji Watanabe[4], Takashi Taniguchi[5], Sabine Steil[1], Daniel Steil[1], R Thomas Weitz[1,6], Stephan Hofmann[3], G S Matthijs Jansen[1], Samuel Brem[2], Ermin Malic[2], Marcel Reutzel[1,*] and Stefan Mathias[1,6,*]

[1] I. Physikalisches Institut, Georg-August-Universität Göttingen, Friedrich-Hund-Platz 1, 37077 Göttingen, Germany
[2] Fachbereich Physik, Philipps-Universität, 35032 Marburg, Germany
[3] Department of Engineering, University of Cambridge, Cambridge CB3 0FA, United Kingdom
[4] Research Center for Electronic and Optical Materials, National Institute for Materials Science, 1-1 Namiki, Tsukuba 305-0044, Japan
[5] Research Center for Materials Nanoarchitectonics, National Institute for Materials Science, 1-1 Namiki, Tsukuba 305-0044, Japan
[6] International Center for Advanced Studies of Energy Conversion (ICASEC), University of Göttingen, Göttingen, Germany
[*] Authors to whom any correspondence should be addressed.

E-mail: marcel.reutzel@phys.uni-goettingen.de and smathias@uni-goettingen.de

Keywords: moiré materials, time- and angle-resolved photoelectron spectroscopy, interlayer exciton, hybrid exciton, dark exciton, transition metal dichalcogenide, exciton dynamics

Abstract

The energy landscape of optical excitations in mono- and few-layer transition metal dichalcogenides (TMDs) is dominated by optically bright and dark excitons. These excitons can be fully localized within a single TMD layer, or the electron- and the hole-component of the exciton can be charge-separated over multiple TMD layers. Such intra- or interlayer excitons have been characterized in detail using all-optical spectroscopies, and, more recently, photoemission spectroscopy. In addition, there are so-called hybrid excitons whose electron- and/or hole-component are delocalized over two or more TMD layers, and therefore provide a promising pathway to mediate charge-transfer processes across the TMD interface. Hence, an in-situ characterization of their energy landscape and dynamics is of vital interest. In this work, using femtosecond momentum microscopy combined with many-particle modeling, we quantitatively compare the dynamics of momentum-indirect intralayer excitons in monolayer WSe_2 with the dynamics of momentum-indirect hybrid excitons in heterobilayer WSe_2/MoS_2, and draw three key conclusions: First, we find that the energy of hybrid excitons is reduced when compared to excitons with pure intralayer character. Second, we show that the momentum-indirect intralayer and hybrid excitons are formed via exciton-phonon scattering from optically excited bright excitons. And third, we demonstrate that the efficiency for phonon absorption and emission processes in the mono- and the heterobilayer is strongly dependent on the energy alignment of the intralayer and hybrid excitons with respect to the optically excited bright exciton. Overall, our work provides microscopic insights into exciton dynamics in TMD mono- and bilayers.

1. Introduction

Exfoliated and artificially stacked monolayers of transition metal dichalcogenides (TMDs) have been shown to be a highly tuneable material platform for exploring optical excitations and correlated interactions on the atomic scale [1–7]. After first experiments identified the transition from an indirect to a direct semiconductor when exfoliating bulk TMDs to the monolayer limit [8, 9], subsequent studies characterized the strong exciton response to an optical excitation [10–13]. Importantly, these pioneering all-optical experiments are for the most part only sensitive to radiative recombination processes within the light-cone [14, 15]. However, in addition to these bright excitons, it is meanwhile well-known that

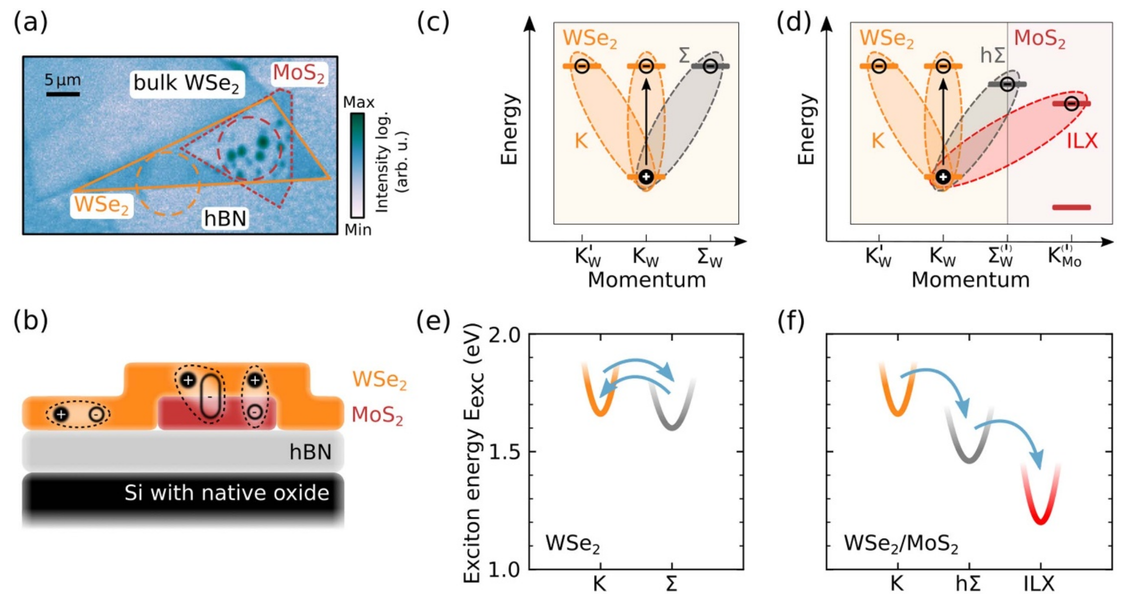

Figure 1. Real-space sample structure and energy landscape of monolayer WSe_2 and heterobilayer WSe_2/MoS_2. (a) Real-space resolved photoemission image of the monolayers WSe_2 (orange polygon) and MoS_2 (dark red dashed polygon). Femtosecond momentum microscopy experiments of the monolayer WSe_2 and the heterobilayer WSe_2/MoS_2 are performed in the regions-of-interest indicated by the orange and dark red circles, respectively. (b) Schematic sketch of the TMD heterostructure after excitation with a 1.7 eV light pulse. Intralayer excitons are formed in the WSe_2 monolayer and the WSe_2/MoS_2 heterobilayer. In the WSe_2/MoS_2 heterostructure, the energetically most stable state is the interlayer exciton where the electron and the hole component are localized in the WSe_2 and the MoS_2 layer, respectively. In addition, hybrid excitons are formed for which the exciton's hole is fully localized in the WSe_2 layer and the exciton's electron has probability density in the WSe_2 and the MoS_2 layer. (c), (d) Single-particle energy landscape of monolayer WSe_2 and heterobilayer WSe_2/MoS_2. The filled bars indicate the single-particle valence and conduction band extrema at the Brillouin zone's high-symmetry points. The ovals indicate the Coulomb correlation between the single-particle electrons and holes, and the letters label the electron–hole pairs, as introduced in the main text. (e), (f) Energy landscape of excitons in the WSe_2 monolayer and the WSe_2/MoS_2 heterobilayer. The energies E_{exc} are obtained in experiment, and the blue arrows indicate the dominant scattering pathways.

also tightly bound dark excitons contribute to the energy landscape of excitons [16–21]. For example, for momentum-indirect dark excitons in a monolayer TMD, the exciton's electron and hole component can reside in different valleys of the TMD Brillouin zone (figures 1(c) and (e)). In the case that TMD homo- and heterostructures are assembled by more than one layer, the situation can become even more complex: The twist-angle between two neighbouring TMD layers can be varied from 0° to 60°, and, in this way, the high-symmetry points of the Brillouin zones are offset in momentum space. Hence, so-called interlayer excitons for which the electron- and the hole-component are charge-separated across the interface are typically momentum-indirect and thus optically dark (figures 1(d) and (f)) [22].

First direct access to these dark excitons has been provided in optical-pump-midinfrared-probe experiments [23, 24]. With the development of high-repetition rate extreme ultraviolet light sources [25–28], time- and angle-resolved photoelectron spectroscopy (trARPES) [29, 30] has become applicable to probe the energetics and dynamics of bright and dark excitons. First experiments focused onto the ultrafast exciton and charge carrier dynamics in semiconducting bulk [31–35] and wafer-scale [36–40] TMDs. More recently, empowered by the development of time-of-flight momentum microscopes (ToF-MMs) [41, 42], trARPES has been successfully applied to probe the formation dynamics of momentum-indirect intralayer excitons [43, 44] and the valley depolarization dynamics [45] in exfoliated monolayer TMDs. In addition, the cascaded exciton transition from bright intralayer to dark interlayer excitons has been quantified in an artificially stacked TMD heterobilayer [46, 47].

These seminal trARPES experiments of exfoliated TMDs all focus on excitons that are either of full intra- or interlayer character: The exciton's electron and hole either reside both in a single TMD layer, or are charge-separated between both layers. Until today, no trARPES experiment has focused on the case where hybridization between the neighbouring TMD layers leads to the formation of a new type of exciton where either the electron-, the hole-, or the electron- and the hole-component are delocalized between both layers (figure 1(b)). Importantly, these so-called hybrid excitons are of great interest due to their potential to mediate charge transfer across a TMD interface [34, 46, 48–52]. Moreover, they have a high oscillator strength and a sensitivity to external electrical fields due to their partial intra- and interlayer character [20, 53–59].

In this article, we study the effect of interlayer hybridization on the energy landscape of excitons and the resulting femto- to picosecond dynamics. We follow-up on our recent work [46], where we have studied the ultrafast exciton dynamics in heterobilayer WSe_2/MoS_2 and found that interlayer excitons are formed in a step-wise process via intermediate hybrid excitons. Here, we directly compare the impact of layer-localized Σ excitons in a monolayer WSe_2 with hybrid $h\Sigma$ excitons in a heterobilayer WSe_2/MoS_2 on the exciton dynamics. For both excitons, the hole-component to the exciton is fully layer-localized and found in the K_W valley valence band maximum (VBM) of WSe_2. In contrast, the exciton's electron, which resides in the Σ valley of the conduction band, is either fully layer localized (WSe_2) or has a significant degree of interlayer hybridization (WSe_2/MoS_2). First, we experimentally quantify the bright and dark exciton energies E^i_{exc} of the correlated two-particle energy landscape. Second, we identify exciton-phonon scattering as the dominating mechanism for the formation of intralayer Σ and hybrid $h\Sigma$ excitons. And third, we show that the sub-ps exciton thermalization dynamics are significantly affected by the energy alignment of the Σ and $h\Sigma$ exciton with respect to the optically excited exciton.

2. Bright and dark excitons in WSe_2 and WSe_2/MoS_2

The major goal of this manuscript is the identification of hybrid excitons in the trARPES experiment and the evaluation of their impact on the exciton relaxation dynamics. Therefore, we describe the low energy landscape of excitons as calculated by solving the Wannier equation [6, 20, 21, 49, 60, 61]. All relevant excitation energies are summarized in the energy diagrams in figures 1(c)–(f) and table 1. The calculations are performed on the same basis as in our previous works for monolayers [61] and heterobilayers [46].

If the monolayer WSe_2 is pumped with 1.7 eV photons, bright A1s excitons of WSe_2 are resonantly excited (black arrow in figure 1(c)). We label this exciton as K as its electron and hole component reside in the K_W valley conduction band minimum and VBM, respectively. Note that throughout the manuscript, we do not differentiate between K excitons that are bound at K_W or K'_W valleys, because we cannot distinguish them in experiment. In addition to the bright A1s exciton, two distinct momentum-indirect dark excitons can be formed in a subsequent scattering process: On the one hand, there are momentum-indirect dark excitons for which the electron- and the hole-component are found in the Σ_W and the K_W valleys, respectively; these excitons are labelled as Σ throughout our work (figures 1(c) and (e)). On the other hand, momentum-indirect excitons for which the electron- and the hole-component are momentum-offset and found in the K_W or K'_W valleys can be formed. Importantly, while it is expected that these momentum-indirect excitons are energetically favourable over the optically excited bright excitons [21, 57, 58], where the electron- and the hole-component are bound in the same K_W or K'_W valley, within the energy resolution of the photoemission experiment, it is not possible to separate these excitons. Hence, we label both of them with K throughout the manuscript.

In the WSe_2/MoS_2 heterostructure, 1.7 eV photons can be used to resonantly excite the A1s exciton in WSe_2 (black arrow in figure 1(d)). A similar resonance frequency for the optical excitation of WSe_2 A1s excitons in the mono- and the heterobilayer region can be rationalized based on the fact that wavefunction hybridization at the K_W valleys is negligible [48, 51, 60, 62, 63]. In addition, because the optical excitation of A1s excitons of monolayer MoS_2 would require at least 1.9 eV light-pulses [47, 50, 63, 64], the MoS_2 monolayer is not directly excited. The optically excited WSe_2 A1s excitons can decay to form momentum-indirect excitons, where the electron- and the hole-component are momentum-offset between the K_W and K'_W valleys. Because we cannot differentiate between these momentum-indirect excitons and the bright A1s excitons in the photoemission experiment, as in the case of the WSe_2 monolayer, we label both these bright and momentum-indirect excitons with K. More interestingly for our study, momentum-indirect hybrid $h\Sigma$ excitons are formed for which the exciton's hole and electron can be found in the K_W and the $\Sigma^{(\prime)}$ valley, respectively: Here, the $\Sigma^{(\prime)}$ valley conduction bands of the WSe_2 and MoS_2 are hybridized, and, in consequence, the $h\Sigma$ exciton can be described in the hybrid exciton basis with approximately 30% intra- and 70% interlayer character [46]. Note that the hybrid character of this exciton's electron component is indicated by the letter 'h' in the abbreviation. With this hybrid character of the $h\Sigma$ excitons, interlayer charge transfer is strongly favoured and interlayer excitons (ILX) can be formed [46, 49]. For ILX, because of the negligible hybridization of the wavefunctions at the WSe_2 $K^{(\prime)}_W$ and MoS_2 $K^{(\prime)}_{Mo}$ valleys, the exciton's electron and hole component are again fully localized in the monolayers (figure 1(d)).

3. Momentum microscopy: energy landscape of excitons

In this section, we experimentally quantify the exciton energies of the bright and dark excitons in the WSe_2 monolayer and the WSe_2/MoS_2 heterolayer. All energies are summarized in table 1.

Table 1. Overview of the exciton energies E^{i}_{exc} in monolayer WSe$_2$ and heterobilayer WSe$_2$/MoS$_2$. The table compares experimentally determined values of this work with many-particle calculations (heterobilayer values reproduced from [46]). In addition, exciton energies obtained in photoluminescence (PL) [62] and other trARPES [43, 65] experiments are reproduced. The theory values are calculated based on the model for the mono- and the heterobilayer, as detailed in [46, 61]. Note that the exciton energy of the optically excited bright exciton in the model is adapted to experiment. If two calculated exciton energies are noted, the first is attributed to the exciton where the electron- and the hole-component are found at a high-symmetry point of the Brillouin zone with the same valley degree of freedom (e.g. *KK* excitons). The second value then gives the energy of the exciton where the electron- and the hole-component have different valley degrees of freedom (e.g. *KK*′ excitons).

	Monolayer WSe$_2$		Heterobilayer WSe$_2$/MoS$_2$		PL	trARPES	trARPES
	Experiment	Theory	Experiment	Theory [46]	Reference [62]	Reference [43]	Reference [65]
$E^{\mathrm{K}}_{\mathrm{exc}}$ (eV)	1.67 ± 0.05	1.67 and 1.61	1.66 ± 0.05	1.66 and 1.61	1.66	1.73	—
$E^{\Sigma}_{\mathrm{exc}}$ (eV)	1.60 ± 0.05	1.62 and 1.83	—	—	—	1.73	—
$E^{\mathrm{h}\Sigma}_{\mathrm{exc}}$ (eV)	—	—	1.46 ± 0.05	1.37 and 1.48	—	—	—
$E^{\mathrm{ILX}}_{\mathrm{exc}}$ (eV)	—	—	1.20 ± 0.05	1.24 and 1.25	1.05	—	≈1.1

3.1. Femtosecond momentum microscopy of exfoliated TMDs

In order to establish the most direct experimental comparison of the exciton energy landscape of the WSe$_2$ monolayer and the twisted WSe$_2$/MoS$_2$ heterobilayer, we fabricate a single sample that contains distinct areas in which the monolayer WSe$_2$ flake and the WSe$_2$/MoS$_2$ heterostructure are found (figure 1(a)). We have chosen a doped silicon wafer with a native oxide layer as the substrate for the heterostructure, because it ensures high quality trARPES data that is not affected by sample charging (figure 1(b)). Moreover, the TMD flakes are stacked on 20–30 nm hexagonal boron nitride [66] for best interface quality [67]. Before the trARPES experiments, the sample is annealed for 1 h to 670 K. In the real-space-resolved photoemission electron microscopy image in figure 1(a), the boundaries of the WSe$_2$ and MoS$_2$ monolayers are traced by orange and dark red (dashed) polygons, respectively. The twist-angle of the heterostructure is quantified to $9.8 \pm 0.8°$ [46].

Time-resolved photoemission spectroscopy of exfoliated mono- and heterobilayers becomes possible by using our setup for femtosecond momentum microscopy (see [25, 68, 69]). We resonantly excite the bright A1s exciton of WSe$_2$ with 1.7 eV 40 fs light pulses (*s*-polarized). Photoemission from the occupied band structure and the excitons is induced with time-delayed 26.5 eV 20 fs light pulses (*p*-polarized) that are created in a table-top 500 kHz repetition rate high-harmonic generation beamline [25, 70, 71]. For each delay between the pump and the probe laser pulse, the ToF-MM (Surface Concept GmbH) collects three-dimensional data cubes that contain information on the two in-plane momenta k_x and k_y and the energy E of the detected photoelectrons [25, 42]. Notably, by inserting an aperture into the real-space plane of the microscope, the experiment is sensitive to the exciton dynamics in a sample region with a diameter of 10 μm (orange and red circles in figure 1(a)) [43–46].

The momentum microscopy experiment can be used to directly characterize and compare the occupied band structure of monolayer WSe$_2$ and heterobilayer WSe$_2$/MoS$_2$ (figure 2). In both sample areas, the spin-split valence bands at the WSe$_2$ K_{W} valley can be identified (labelled (1) and (2) in the magenta energy-distribution-curves (EDCs)). For the characterization of the inhomogeneity of the heterostructure, we analyse the linewidth of the top WSe$_2$ valence band at the K_{W} valley, and find a full width at half maximum of ≈280 meV (figure 2(b)). The linewidth is composed of the spectral width of the probe laser pulse (≈200 meV) and inhomogeneous broadening of about ≈200 meV due to imperfections and inhomogeneities within the probed sample area ($\approx 100 \mu m^2$) [46, 72]. In the heterobilayer, in addition, the MoS$_2$ valence band is observed at $E - E_{\mathrm{VBM}} = 0.94 \pm 0.05$ eV (labelled (3) in figure 2(b)). While the dispersion of the WSe$_2$ valence bands are similar at the K_{W} valleys of the mono- and the heterobilayer, it is strikingly different at the Γ valley: In the monolayer, only a single band at the Γ valley is observed (horizontal arrow, figure 2(a)). In contrast, in the heterobilayer, we find two energetically separated bands that are a clear indication for interlayer hybridization (two horizontal arrows in figure 2(b)) [73–75].

3.2. Spectroscopy of excitons in monolayer WSe$_2$ and heterobilayer WSe$_2$/MoS$_2$

Having identified these distinct spectroscopic signatures of the electronic band structure that allow the direct discrimination of the mono- and the heterobilayer region in the trARPES experiment, in the next step, we probe the energetics of the optical excitations of the WSe$_2$ monolayer. Therefore, optical pump pulses with a centre energy of 1.7 eV are used in order to be resonant to the WSe$_2$ A1s exciton (fluence: 280 μJ cm^2, exciton density: 5.4×10^{12} excitons cm^2). We find spectral weight above the valence bands that we attribute to photoelectrons being emitted from excitons (figure 2(a)). Specifically, at a pump-probe delay of 1 ps, photoemission yield is detected at the

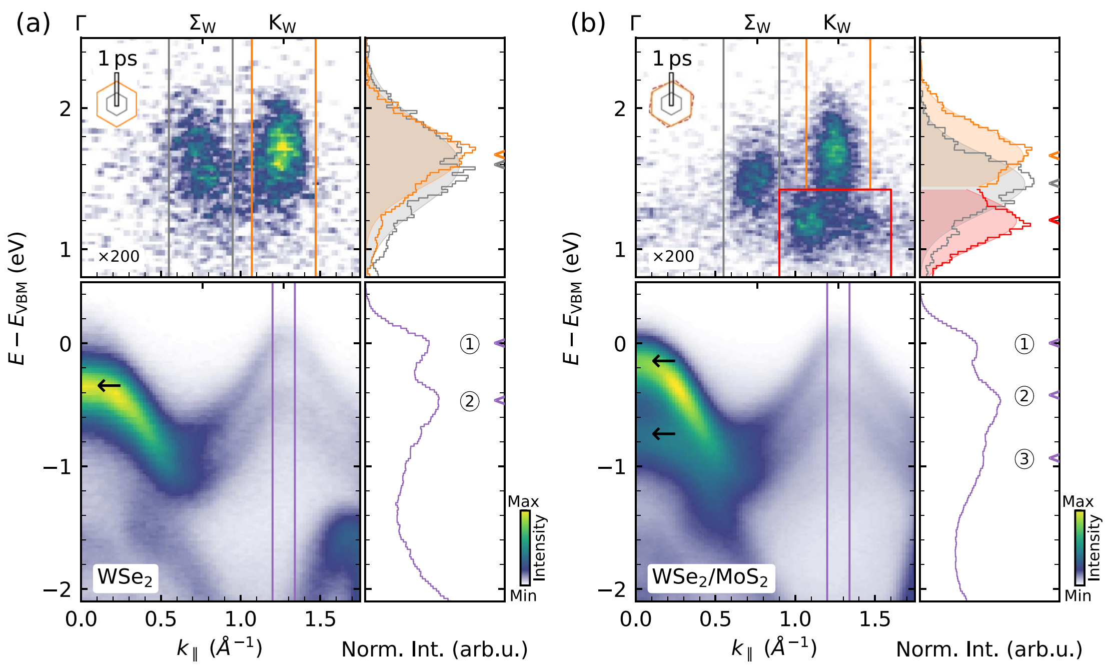

Figure 2. Energy- and momentum-resolved photoemission spectra of monolayer WSe_2 and heterobilayer WSe_2/MoS_2 along the Γ-K_W direction (inset). (a) The occupied valence band structure of monolayer WSe_2 is dominated by a single-band at the Γ valley (black horizontal arrow) and the spin-split valence bands at the K_W valley (labelled (1) and (2) in the EDC). At a pump-probe delay of 1 ps and a photoemission energy of $\approx$1.7 eV, exciton photoemission yield from intralayer K (orange) and Σ (grey) excitons is detected. (b) The occupied valence band structure of heterobilayer WSe_2/MoS_2 is characterized by the WSe_2 spin-split valence bands at the K_W valley (labelled (1) and (2) in the EDCs) and the valence band of MoS_2 (3), for which the spin-splitting is not resolved. At the Γ valley, interlayer hybridization leads to the formation of two bands (horizontal black arrows). At a pump-probe delay of 1 ps, exciton photoemission yield is detected from the intralayer K excitons (orange), hybrid $h\Sigma$ excitons (grey) and ILX (red). The photoemission energy from hybrid $h\Sigma$ exciton's is significantly reduced when compared to the intralayer K (monolayer and heterobilayer) and Σ (monolayer) excitons. The energy-momentum cuts are obtained by summation of all six measured Γ–K_W (Γ–K'_W) directions.

K_W and the Σ_W valleys of the WSe_2 Brillouin zone (orange and grey hexagon in figure 3(a), respectively). These spectral signatures can be attributed to photoemission from intralayer K and Σ excitons, consistent with earlier reports [43, 44].

When applying similar excitation conditions to the WSe_2/MoS_2 heterobilayer region, much richer spectral signatures are detected in the momentum microscopy experiment: A complex distribution of photoemission intensity is detected above the WSe_2 valence bands in an energy window ranging from 0.9 eV to 1.9 eV (figure 2(b), 1 ps pump-probe delay). The momentum-map centred at an energy of 1.7 eV above the WSe_2 VBM shows spectral weight at the momenta of the K_W and the Σ_W valleys that we attribute to photoemission signal from intralayer K and hybrid $h\Sigma$ excitons (figure 3(b), orange and grey hexagon, respectively). At a lower energy (figure 3(c), $E - E_{VBM} \approx 1.1$ eV), we find a complex momentum structure of the photoemission intensity that can be attributed to ILX: Spectral weight is detected at the K_{Mo} valley and the additional κ valleys that are described within the moiré mini Brillouin zone (mBz, red hexagon). This hallmark of the moiré superlattice imprinted onto the exciton photoemission signature from the interlayer ILX excitons is discussed in detail in [46].

3.3. Energy landscape of excitons in WSe_2 and WSe_2/MoS_2

Having identified the major photoemission spectral signatures of excitons, we aim to experimentally quantify the energy landscape of bright and dark excitons in the mono- and the heterobilayer sample. For this, first, we have to discuss at which energy the photoemission experiment detects single-particle photoelectrons that have initially been bound in the correlated exciton state. In the process of photoemission from an exciton, the Coulomb correlation between the exciton's electron and hole is broken at the cost of the exciton binding energy. As described by Weinelt *et al* [76] and others [35, 47, 77–84], the single-particle photoelectron from an exciton will be detected one exciton energy E^i_{exc} above the energy of the single-particle band where the former hole contribution to the exciton remains in the sample, i.e. at

$$E_{elec} = E_{hole} + E^i_{exc} + \hbar\omega \quad (1)$$

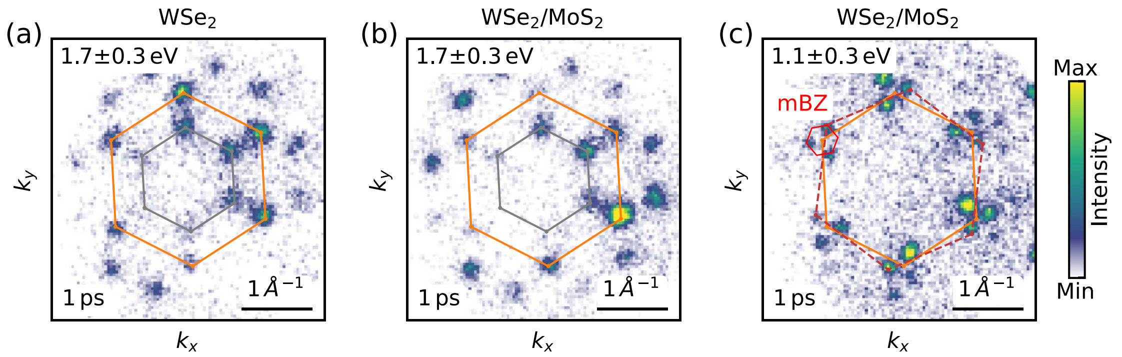

Figure 3. Momentum-resolved photoemission maps at the energies of the intralayer, hybrid and interlayer excitons in monolayer WSe_2 and heterobilayer WSe_2/MoS_2. The pump-probe delay and the photoemission energy with respect to the WSe_2 VBM are given in the figure. All momentum maps are integrated in an energy window ± 0.3 eV around the centre energy. (a) In the WSe_2 monolayer, the exciton photoemission momentum fingerprints of intralayer K (orange) and Σ (grey) show spectral weight at the $K_W^{(\prime)}$ and $\Sigma_W^{(\prime)}$ valleys of the WSe_2 hexagonal Brillouin zone. (b) In the WSe_2/MoS_2 heterobilayer, exciton photoemission from the intralayer K (orange) and the hybrid $h\Sigma$ (grey) excitons is found at the $K_W^{(\prime)}$ and $\Sigma_W^{(\prime)}$ valleys of the WSe_2 hexagonal Brillouin zones. (c) The momentum-misalignment of the Brillouin zones of WSe_2 (orange hexagon) and MoS_2 (dark red dashed hexagon) leads to a complex photoemission signature from ILX that can be described within the moiré mini Brillioun zone (mBZ, red hexagon).

with E_{hole} and E_{elec} as the single-particle energy of the hole- and the electron-state, respectively; furthermore with E^i_{exc} as the exciton energy and $\hbar\omega$ as the probe photon energy. Importantly, equation (1) sets the energy of the WSe_2 VBM at the K_W valley as the natural reference point of the present experiment, because the single-particle hole of all probed excitons remains in this valley once photoemission has occurred (see figures 2(c) and (d)).

Hence, we can quantify the exciton energy E^i_{exc} of all contributing intralayer, hybrid and interlayer excitons by analysing the EDCs taken at the K_W, the Σ_W and the K_{Mo} (κ) valleys (figure 2). Following equation (1), we then calculate the energy difference between each exciton photoemission signal and the energy of the K_W valley VBM. All exciton energies E^i_{exc} quantified for the WSe_2 mono- and the WSe_2/MoS_2 heterobilayer are summarized in table 1. In addition, previous experimentally determined exciton energies extracted by photoluminescence (PL) [62] and trARPES [43, 65] are summarized in table 1, and show an excellent agreement with our analysis.

Having experimentally measured the exciton energies E^i_{exc}, we are now in the position to systematically compare those values. First, we find that, within the experimental error, the intralayer K exciton energy is comparable in the mono- and the heterobilayer region (1.67 ± 0.05 eV vs. 1.66 ± 0.05 eV). For WSe_2/MoS_2, this result strongly supports the expectation that excitons, where the electron- and hole-component are localized in the K_W valleys, are not affected by interlayer hybridization [48, 51, 60]. In contrast, we find that the hybrid character of the $h\Sigma$ excitons indeed leads to a renormalization of the exciton energy: The interlayer hybridization leads to a reduction of the exciton energy from 1.60 ± 0.05 eV (Σ exciton, monolayer WSe_2) to 1.46 ± 0.05 eV ($h\Sigma$ exciton, heterobilayer WSe_2/MoS_2). This observation is a direct experimental verification of seminal photoluminescence experiments that reported a changed emission energy for hybrid excitons, if the degree of hybridization is controlled, e.g. by the twist angle [51, 85–87]. Moreover, it fully confirms the calculated energy landscape of excitons that predicts a reduction of the energy of the hybrid $h\Sigma$ exciton of the WSe_2/MoS_2 heterobilayer in comparison to the intralayer Σ exciton of the WSe_2 monolayer (table 1).

4. Ultrafast exciton dynamics in WSe_2 and WSe_2/MoS_2

Having characterized the energy landscape of excitons, we now turn to the exciton scattering dynamics. Specifically, the goal of the analysis is to pinpoint the impact of the intralayer Σ and hybrid $h\Sigma$ excitons on the relaxation dynamics. Therefore, first, we compare the experimentally measured exciton dynamics with microscopic many-particle calculations that allow us to identify exciton-phonon scattering as the dominant mechanism for intervalley thermalization and the formation of the intralayer Σ and hybrid $h\Sigma$ excitons. Second, we focus on the sub-ps dynamics in order to elucidate the impact of the different exciton energies of the intralayer Σ and the hybrid $h\Sigma$ exciton on the exciton relaxation cascade.

4.1. Exciton-phonon scattering: Formation of intralayer Σ and hybrid $h\Sigma$ excitons

The femtosecond momentum microscopy experiment provides direct access to the ultrafast dynamics of bright and dark excitons. The symbols in the main panels of figure 4 show the pump-probe delay-dependent photoemission yield from the intralayer K (orange), intralayer Σ (grey), hybrid $h\Sigma$ (grey)

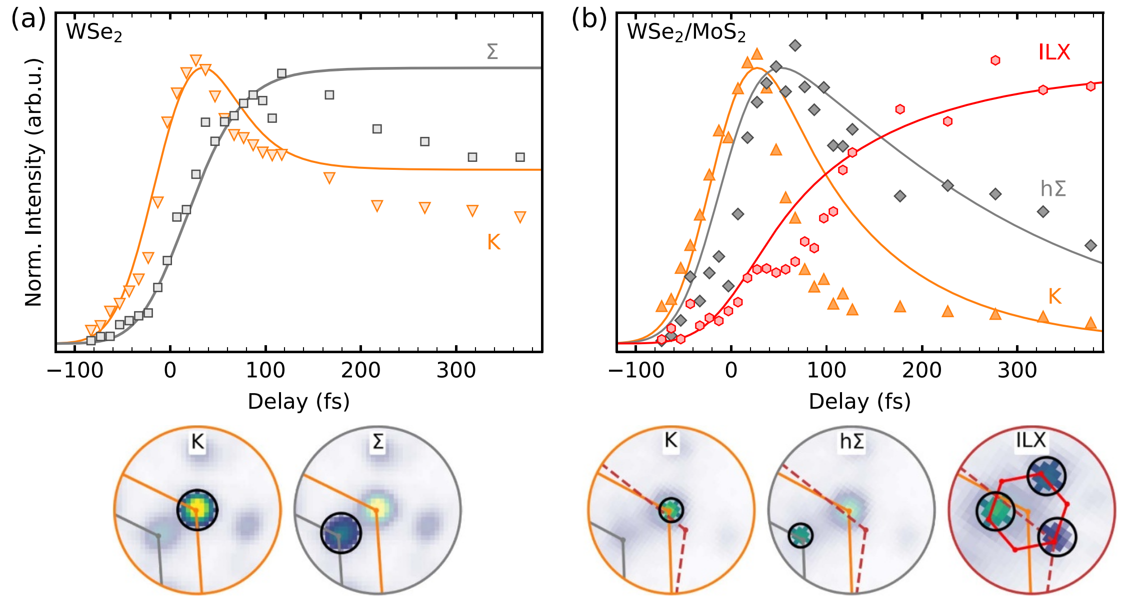

Figure 4. Direct comparison of the ultrafast exciton dynamics in (a) monolayer WSe_2 and (b) heterobilayer WSe_2/MoS_2. The symbols show the pump-probe delay-dependent photoemission yield from excitons, and the solid lines are based on microscopic calculations. The exciton photoemission yield is filtered in the black-circled regions-of-interest indicated in the momentum-maps.

and ILX (red) excitons. In addition, the femtosecond evolution of exciton occupation as calculated in our microscopic model is plotted as solid lines of the respective colour.

In the WSe_2 monolayer (figure 4(a)), photoemission yield from the K exciton peaks at pump-probe delays close to 40 fs. Delayed to this process, we find that spectral weight from momentum-indirect Σ excitons (grey) increases on a 100 fs timescale. This rise of the photoemission yield from the intralayer Σ excitons is in agreement with momentum microscopy experiments by Madéo *et al* [43] and Wallauer *et al* [44]. Moreover, the rise time is also in agreement with our microscopic calculations that include exciton-light and exciton-phonon interaction. From the model, we therefore identify exciton-phonon scattering as the dominant mechanism for the formation of intralayer Σ excitons. Note that for pump-probe delays >100 fs, the exciton occupation calculated in the model overestimates the experimentally measured photoemisison intensity from both excitons. The reason for this deviation is that the model does not include decay processes and thus overestimates the exciton occupation for longer pump-probe delays.

The pump-probe delay-dependent photoemission yield from excitons measured in the WSe_2/MoS_2 heterobilayer is shown in figure 4(b). We find a direct hierarchy in the onset of rising photoemission yield from the three types of excitons, i.e.the K excitons (orange), the hybrid $h\Sigma$ excitons (grey), and the ILX (red). Again, the dynamics is in excellent agreement with our microscopic calculations, such that we can identify exciton-phonon scattering as the dominant mechanism for the formation of hybrid $h\Sigma$ excitons.

4.2. Monolayer WSe_2: Steady state of phonon emission and absorption processes

So far, we have found that the intervalley relaxation processes in monolayer WSe_2 and heterobilayer WSe_2/MoS_2 are phonon-mediated and lead to the formation of intralayer Σ and hybrid $h\Sigma$ excitons, respectively. However, even though the intervalley relaxation proceeds via the same mechanism, we find distinctly different decay dynamics of the contributing intralayer and hybrid excitons on the sub-ps timescale (figure 5 and table 2). In the following, we pinpoint the origin of the different dynamics to the relative energy alignment of the intralayer Σ and hybrid $h\Sigma$ excitons with respect to the intralayer K excitons, which has direct impact on the efficiency of exciton-phonon scattering processes.

In monolayer WSe_2, the energy difference between the optically excited K and the intralayer Σ exciton is $\Delta E_{\mathrm{exc}}^{\mathrm{WSe_2}} = E_{\mathrm{exc}}^{\mathrm{K}} - E_{\mathrm{exc}}^{\Sigma} = 0.07 \pm 0.10$ eV. Hence, phonon emission and absorption processes with typical energies of 0.03 eV [88] can efficiently create a steady state between both excitonic species, i.e. $K \rightleftharpoons \Sigma$, where the relative exciton occupation is given by degenerate Bose–Einstein distributions [21]. In order to identify this steady state in the photoemission data, we plot the sub-ps pump-probe delay-dependent photoemission intensity from K and Σ excitons on a logarithmic intensity axis in figures 5(a) and (b), respectively. As indicated by the yellow, green and blue marked areas, the sub-ps dynamics of K excitons can be divided into overall three characteristic timescales. On the sub-40-fs timescale (yellow, figure 5(a)), photoemission yield

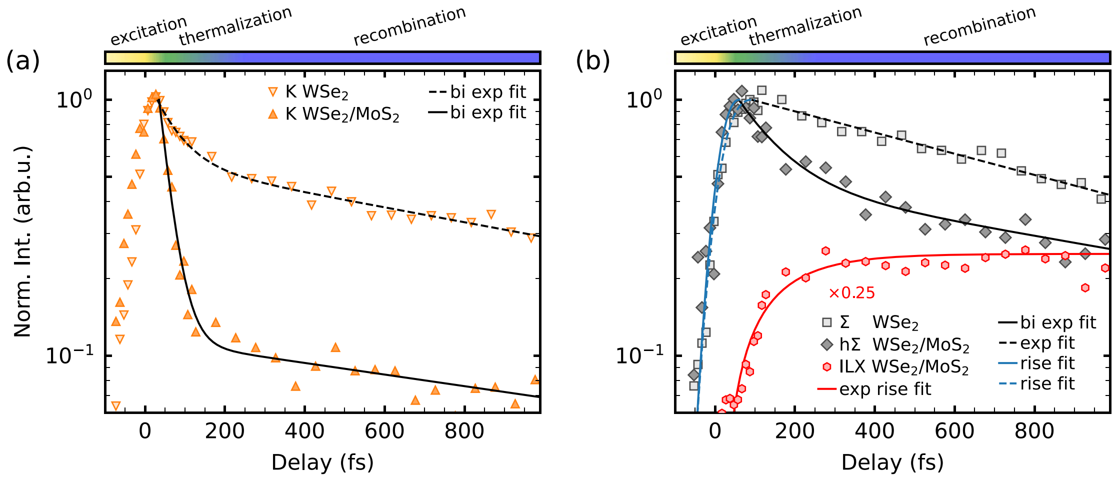

Figure 5. Quantitative analysis of the intralayer and hybrid exciton dynamics. In the yellow, green and blue shaded delay regions, excitons are optically excited, thermalize and radiatively recombine, respectively. (a) Pump-probe-delay evolution of photoemission signal from K excitons in monolayer WSe$_2$ (empty triangles) and heterobilayer WSe$_2$/MoS$_2$ (filled triangles); the dashed and solid lines are bi-exponential decay fits to the data. (b) Quantitative evaluation of the formation and relaxation dynamics of intralayer Σ excitons (empty squares, grey) and hybrid $h\Sigma$ excitons (filled squares, grey). The rise time of the excitons is evaluated with a one-level rate equation model (blue dashed and solid line, respectively). The decay dynamics is approximated by bi- and single-exponential fits, respectively. The rise time of the ILX (red circles) is fitted with a single exponential function (red line). All rise and decay constants are summarized in table 2.

from K excitons increases due to the optical excitation. For increasing pump-probe delay, the decaying photoemission intensity can be approximated by a bi-exponential function. Here, the two decay times $\tau^{K}_{\mathrm{WSe_2,fast}} = 70 \pm 10$ fs and $\tau^{K}_{\mathrm{WSe_2,slow}} = 1.5 \pm 0.2$ ps describe the fast and the slow component of the dynamics that are dominant in the green and blue delay-regions, respectively. In direct comparison to time-resolved all-optical spectroscopies, the slow component $\tau^{K}_{\mathrm{WSe_2,slow}}$ can be attributed to radiative recombination processes of the bright excitons [50, 63, 89]. However, the interpretation of the fast time constant $\tau^{K}_{\mathrm{WSe_2,fast}}$ is more complex (green): First, it contains information on the decay of the coherent exciton polarization towards the incoherent K exciton population [44, 90], which is not the focus of our study. Second, and more importantly, $\tau^{K}_{\mathrm{WSe_2,fast}}$ is dominant in the delay-window that is necessary to establish a steady state between phonon absorption and emission events transferring K into Σ excitons and vice versa. In agreement with this assignment, we find that photoemission intensity from momentum-indirect Σ excitons, which are formed due to the decay of K excitons, rises on the same timescale and peaks at 100 fs (yellow and green delay-region in figure 5(b)). For longer delays (blue delay-region), the Σ exciton photoemission intensity decays and is described by a single-exponential fit with a decay time of $\tau^{\Sigma}_{\mathrm{WSe_2}} = 1.1 \pm 0.1$ ps. Notably, it has already been suggested that the decay of momentum-indirect Σ excitons dominantly proceeds via phonon absorption processes that first transfer the Σ excitons into bright K excitons that can, subsequently, decay in a radiative process [15, 21, 91]. Our analysis verifies this proposition, because the experimentally quantified decay time $\tau^{\Sigma}_{\mathrm{WSe_2}}$ of dark Σ excitons is in reasonable agreement with the radiative decay time $\tau^{K}_{\mathrm{WSe_2,fast}}$ of K excitons (cf table 2).

4.3. Heterobilayer WSe$_2$/MoS$_2$: Phonon emission processes and formation of interlayer excitons

The situation is significantly different for the WSe$_2$/MoS$_2$ heterobilayer. The hybrid character of the $h\Sigma$ exciton leads to a reduction of its exciton energy and thus to an energy difference of $\Delta E^{\mathrm{WSe_2/MoS_2}}_{\mathrm{exc}} = E^{K}_{\mathrm{exc}} - E^{h\Sigma}_{\mathrm{exc}} = 0.20 \pm 0.10$ eV with respect to the intralayer K exciton. Hence, accompanied by the emission of a phonon, optically excited K excitons can effectively be transferred to hybrid $h\Sigma$ excitons. However, the large energy difference $\Delta E^{\mathrm{WSe_2/MoS_2}}_{\mathrm{exc}}$ strongly suppresses backscattering events for which multiple phonon absorption processes would be required. The suppression of the backscattering channel in the heterobilayer in comparison to the monolayer is most evident by the much stronger reduction of photoemission intensity from K exctions to below 10% after only 100 fs (green delay-region in figure 5(a)). Photoemission intensity from hybrid $h\Sigma$ excitons, on the other side, rises on the same timescale, which is in agreement with the interpretation of an initially fast transfer of excitons from K to $h\Sigma$ excitons (yellow and green delay-regions in figure 5(b)).

Table 2. Summary of the experimentally quantified rise and decay times of photoemission yield from excitons.

	Monolayer WSe_2	Heterobilayer WSe_2/MoS_2
τ^{K}_{fast} (fs)	70 ± 10	28 ± 2
τ^{K}_{slow} (fs)	1500 ± 200	1900 ± 800
$\tau^{\Sigma}_{WSe_2}$ (fs)	1050 ± 60	—
$\tau^{h\Sigma}_{WSe_2/MoS_2,\text{fast}}$ (fs)	—	110 ± 40
$\tau^{h\Sigma}_{WSe_2/MoS_2,\text{slow}}$ (fs)	—	1600 ± 800
$\tau^{\Sigma}_{\text{rise}}$ (fs)	36 ± 3	—
$\tau^{h\Sigma}_{\text{rise}}$ (fs)	—	34 ± 3
$\tau^{\text{ILX}}_{\text{rise}}$ (fs)	—	120 ± 20

Once the hybrid $h\Sigma$ excitons are formed, they can relax to the ILX by subsequent exciton-phonon scattering processes within the MoS_2 layer. For the analysis of this process, we fit the picosecond evolution of photoemission intensity from hybrid $h\Sigma$ excitons with a biexponential function (figure 5(b)) and extract a fast $h\Sigma \rightarrow$ILX decay time of $\tau^{h\Sigma}_{WSe_2/MoS_2,\text{fast}} = 110 \pm 40$ fs. Notably, this decay time is in excellent agreement with the rise time of photoemission intensity from ILX (figure 5(b), $\tau^{\text{ILX}}_{WSe_2/MoS_2,\text{rise}} = 120 \pm 20$ fs, red data points), being thus a strong indication that ILX excitons are directly formed from hybrid $h\Sigma$ excitons. Again, because of the large energy difference between the hybrid $h\Sigma$ exciton and the ILX, i.e. $\Delta E^{\text{ILX}}_{\text{exc}} = E^{h\Sigma}_{\text{exc}} - E^{\text{ILX}}_{\text{exc}} = 0.26 \pm 0.10$ eV (cf table 1), phonon absorption processes are nearly fully suppressed and backscattering events from ILX to hybrid $h\Sigma$ excitons can also be excluded.

Finally, we note that our experimental observation on the efficiency of forward and backward scattering in the WSe_2 monolayer and the WSe_2/MoS_2 heterobilayer are fully consistent with our microscopic model. Specifically, for the WSe_2 monolayer, the calculations reproduce the establishment of a steady state $K \rightleftharpoons \Sigma$ (blue arrows in figure 1(e)). Notably, the model here finds that especially the momentum-indirect excitons, where the hole- and the electron-component are momentum-offset in the K_W and K'_W valleys, contribute to the establishment of the steady state, as detailed, e.g. in [15, 21]. In addition, for the WSe_2/MoS_2 heterobilayer, the microscopic model reproduces the negligible efficiency for backscattering as compared to the forward scattering leading to the formation of ILX (blue arrows in figure 1(f)).

5. Conclusion

In a joint experiment-theory effort, we have used femtosecond momentum microscopy and microscopic modelling to characterize the energy landscape of bright and dark excitons and the resulting scattering dynamics in monolayer WSe_2 and heterobilayer WSe_2/MoS_2. First, we find that interlayer hybridization in WSe_2/MoS_2 leads to a reduction of the energy of the optically dark hybrid exciton when compared to monolayer WSe_2, where the exciton is localized in the layer. Second, in direct comparison to microscopic modelling, we demonstrate that the hybrid $h\Sigma$ and the intralayer Σ excitons are formed via exciton-phonon scattering. And third, we show that the relative efficiency of phonon absorption and emission processes are the dominant parameter for the different exciton dynamics in monolayer WSe_2 and heterobilayer WSe_2/MoS_2. Specifically, in monolayer WSe_2, we showed that the occupation of intralayer K and Σ evolves into a steady state, i.e. $K \rightleftharpoons \Sigma$, and the overall exciton occupation decays via radiative processes of the bright K excitons. In contrast, in the WSe_2/MoS_2 heterobilayer, we found that the energy level alignment of the contributing excitons strongly suppresses phonon-absorption processes and leads to a true exciton cascade $K \rightarrow h\Sigma \rightarrow$ILX with negligible contributions of backscattering.

Data availability statement

The data that support the findings of this study are available upon reasonable request from the authors.

Acknowledgments

This work was funded by the Deutsche Forschungsgemeinschaft (DFG, German Research Foundation) - 432680300/SFB 1456, Project B01, 217133147/SFB 1073, Projects B07 and B10, and 223848855/SFB 1083, Project B9. A A and S H acknowledge funding from EPSRC (EP/T001038/1, EP/P005152/1). A A acknowledges financial support by the Saudi Arabian Ministry of Higher Education. E M acknowledges support from the European Unions Horizon 2020 research and innovation programme under Grant Agreement No. 881603 (Graphene Flagship). K W and T T acknowledge support from the JSPS KAKENHI (Grant Numbers 20H00354, 21H05233 and 23H02052) and World

Premier International Research Center Initiative (WPI), MEXT, Japan.

ORCID iDs

Jan Philipp Bange https://orcid.org/0000-0002-7355-8641
Wiebke Bennecke https://orcid.org/0000-0001-9963-7527
Giuseppe Meneghini https://orcid.org/0000-0002-1889-2380
Marco Merboldt https://orcid.org/0000-0002-8958-7711
Kenji Watanabe https://orcid.org/0000-0003-3701-8119
Daniel Steil https://orcid.org/0000-0001-7448-1167
R Thomas Weitz https://orcid.org/0000-0001-5404-7355
Stephan Hofmann https://orcid.org/0000-0001-6375-1459
G S Matthijs Jansen https://orcid.org/0000-0003-4753-3173
Samuel Brem https://orcid.org/0000-0001-8823-1302
Marcel Reutzel https://orcid.org/0000-0002-1085-2931
Stefan Mathias https://orcid.org/0000-0002-1255-521X

References

[1] Jin C, Ma E Y, Karni O, Regan E C, Wang F and Heinz T F 2018 Ultrafast dynamics in van der Waals heterostructures *Nat. Nanotechnol.* **13** 994–1003

[2] Rivera P, Yu H, Seyler K L, Wilson N P, Yao W and Xu X 2018 Interlayer valley excitons in heterobilayers of transition metal dichalcogenides *Nat. Nanotechnol.* **13** 1004–15

[3] Kennes D M, Claassen M, Xian L, Georges A, Millis A J, Hone J, Dean C R, Basov D N, Pasupathy A N and Rubio A 2021 Moiré heterostructures as a condensed-matter quantum simulator *Nat. Phys.* **17** 155–63

[4] Wilson N P, Yao W, Shan J and Xu X 2021 Excitons and emergent quantum phenomena in stacked 2D semiconductors *Nature* **599** 383–92

[5] Regan E C, Wang D, Paik E Y, Zeng Y, Zhang L, Zhu J, MacDonald A H, Deng H and Wang F 2022 Emerging exciton physics in transition metal dichalcogenide heterobilayers *Nat. Rev. Mater.* **7** 778–95

[6] Perea-Causin R, Erkensten D, Fitzgerald J M, Thompson J J P, Rosati R, Brem S and Malic E 2022 Exciton optics, dynamics and transport in atomically thin semiconductors *APL Mater.* **10** 100701

[7] Raja A *et al* 2018 Enhancement of exciton–phonon scattering from monolayer to bilayer WS_2 *Nano Lett.* **18** 6135–43

[8] Mak K F, Lee C, Hone J, Shan J and Heinz T F 2010 Atomically thin MoS_2: A new direct-gap semiconductor *Phys. Rev. Lett.* **105** 136805

[9] Splendiani A, Sun L, Zhang Y, Li T, Kim J, Chim C-Y, Galli G and Wang F 2010 Emerging photoluminescence in monolayer MoS_2 *Nano Lett.* **10** 1271–5

[10] Wang G, Chernikov A, Glazov M M, Heinz T F, Marie X, Amand T and Urbaszek B 2018 Colloquium: Excitons in atomically thin transition metal dichalcogenides *Rev. Mod. Phys.* **90** 021001

[11] Chernikov A, Berkelbach T C, Hill H M, Rigosi A, Li Y, Aslan O B, Reichman D R, Hybertsen M S and Heinz T F 2014 Exciton binding energy and nonhydrogenic rydberg series in monolayer WS_2 *Phys. Rev. Lett.* **113** 076802

[12] He K, Kumar N, Zhao L, Wang Z, Mak K F, Zhao H and Shan J 2014 Tightly bound excitons in monolayer WSe_2 *Phys. Rev. Lett.* **113** 026803

[13] Ye Z, Cao T, O'Brien K, Zhu H, Yin X, Wang Y, Louie S G and Zhang X 2014 Probing excitonic dark states in single-layer tungsten disulphide *Nature* **513** 214–8

[14] Yu H, Wang Y, Tong Q, Xu X and Yao W 2015 Anomalous Light Cones and Valley Optical Selection Rules of Interlayer Excitons in Twisted Heterobilayers *Phys. Rev. Lett.* **115** 187002

[15] Brem S, Ekman A, Christiansen D, Katsch F, Selig M, Robert C, Marie X, Urbaszek B, Knorr A and Malic E 2020 Phonon-assisted photoluminescence from indirect excitons in monolayers of transition-metal dichalcogenides *Nano Lett.* **20** 2849–56

[16] Zhang X-X, You Y, Zhao S Y F and Heinz T F 2015 Experimental evidence for dark excitons in monolayer WSe_2 *Phys. Rev. Lett.* **115** 257403

[17] Christiansen D *et al* 2017 Phonon sidebands in monolayer transition metal dichalcogenides *Phys. Rev. Lett.* **119** 187402

[18] Selig M, Berghäuser G, Raja A, Nagler P, Schüller C, Heinz T F, Korn T, Chernikov A, Malic E and Knorr A 2016 Excitonic linewidth and coherence lifetime in monolayer transition metal dichalcogenides *Nat. Commun.* **7** 13279

[19] Malic E, Selig M, Feierabend M, Brem S, Christiansen D, Wendler F, Knorr A and Berghäuser G 2018 Dark excitons in transition metal dichalcogenides *Phys. Rev. Mater.* **2** 014002

[20] Deilmann T and Thygesen K S 2019 Finite-momentum exciton landscape in mono- and bilayer transition metal dichalcogenides *2D Mater.* **6** 035003

[21] Selig M, Berghäuser G, Richter M, Bratschitsch R, Knorr A and Malic E 2018 Dark and bright exciton formation, thermalization and photoluminescence in monolayer transition metal dichalcogenides *2D Mater.* **5** 035017

[22] Nayak P K *et al* 2017 Probing evolution of twist-angle-dependent interlayer excitons in $MoSe_2/WSe_2$ van der waals heterostructures *ACS Nano* **11** 4041–50

[23] Poellmann C, Steinleitner P, Leierseder U, Nagler P, Plechinger G, Porer M, Bratschitsch R, Schüller C, Korn T and Huber R 2015 Resonant internal quantum transitions and femtosecond radiative decay of excitons in monolayer WSe_2 *Nat. Mater.* **14** 889–93

[24] Merkl P *et al* 2019 Ultrafast transition between exciton phases in van der Waals heterostructures *Nat. Mater.* **18** 691–6

[25] Keunecke M *et al* 2020 Time-resolved momentum microscopy with a 1 MHz high-harmonic extreme ultraviolet beamline *Rev. Sci. Instrum.* **91** 063905

[26] Puppin M *et al* 2019 Time- and angle-resolved photoemission spectroscopy of solids in the extreme ultraviolet at 500 kHz repetition rate *Rev. Sci. Instrum.* **90** 023104

[27] Heyl C M, Güdde J, L'Huillier A and Höfer U 2012 High-order harmonic generation with μJ laser pulses at high repetition rates *J. Phys. B: At. Mol. Opt. Phys.* **45** 074020

[28] Li X, Reber M A R, Corder C, Chen Y, Zhao P and Allison T K 2016 High-power ultrafast Yb:fiber laser frequency combs using commercially available components and basic fiber tools *Rev. Sci. Instrum.* **87** 093114

[29] Sobota J A, He Y and Shen Z-X 2021 Angle-resolved photoemission studies of quantum materials *Rev. Mod. Phys.* **93** 025006

[30] Bovensiepen U, Petek H and Wolf M 2012 *Dynamics at Solid State Surfaces and Interfaces* (*Fundamentals*) 1st edn, vol 2 (Weinheim: Wiley)

[31] Bertoni R *et al* 2016 Generation and evolution of spin-, valley- and layer-polarized excited carriers in inversion-symmetric WSe_2 *Phys. Rev. Lett.* **117** 277201

[32] Wallauer R, Reimann J, Armbrust N, Güdde J and Höfer U 2016 Intervalley scattering in MoS_2 imaged by two-photon photoemission with a high-harmonic probe *Appl. Phys. Lett.* **109** 162102

[33] Hein P, Stange A, Hanff K, Yang L X, Rohde G, Rossnagel K and Bauer M 2016 Momentum-resolved hot electron dynamics at the 2H-MoS_2 surface *Phys. Rev.* B **94** 205406

[34] Wallauer R, Marauhn P, Reimann J, Zoerb S, Kraus F, Güdde J, Rohlfing M and Höfer U 2020 Momentum-resolved observation of ultrafast interlayer charge transfer between the topmost layers of MoS_2 *Phys. Rev.* B **102** 125417

[35] Dong S *et al* 2021 Direct measurement of key exciton properties: Energy, dynamics and spatial distribution of the wave function *Nat. Sci.* **1** e10010

[36] Grubišić Čabo A *et al* 2015 Observation of ultrafast free carrier dynamics in single layer MoS_2 *Nano Lett.* **15** 5883–7

[37] Liu F, Ziffer M E, Hansen K R, Wang J and Zhu X 2019 Direct Determination of Band-Gap Renormalization in the Photoexcited Monolayer MoS_2 *Phys. Rev. Lett.* **122** 246803

[38] Lin Y, Chan Y-hao, Lee W, Lu Li-S, Li Z, Chang W-H, Shih C-K, Kaindl R A, Louie S G and Lanzara A 2022 Exciton-driven renormalization of quasiparticle band structure in monolayer MoS_2 *Phys. Rev.* B **106** L081117

[39] Lee W, Lin Y, Lu Li-S, Chueh W-C, Liu M, Li X, Chang W-H, Kaindl R A and Shih C-K 2021 Time-resolved ARPES determination of a quasi-particle band gap and hot electron dynamics in monolayer MoS_2 *Nano Lett.* **21** 7363–70

[40] Aeschlimann S *et al* 2020 Direct evidence for efficient ultrafast charge separation in epitaxial WS_2/graphene heterostructures *Sci. Adv.* **6** eaay0761

[41] Krömker B, Escher M, Funnemann D, Hartung D, Engelhard H and Kirschner J 2008 Development of a momentum microscope for time resolved band structure imaging *Rev. Sci. Instrum.* **79** 053702–7

[42] Medjanik K *et al* 2017 Direct 3D mapping of the Fermi surface and Fermi velocity *Nat. Mater.* **16** 615–21

[43] Madéo J *et al* 2020 Directly visualizing the momentum-forbidden dark excitons and their dynamics in atomically thin semiconductors *Science* **370** 1199–204

[44] Wallauer R *et al* 2021 Momentum-resolved observation of exciton formation dynamics in monolayer WS_2 *Nano Lett.* **21** 5867–73

[45] Kunin A *et al* 2023 Momentum-resolved exciton coupling and valley polarization dynamics in monolayer WS_2 *Phys. Rev. Lett.* **130** 046202

[46] Schmitt D *et al* 2022 Formation of moiré interlayer excitons in space and time *Nature* **608** 499–503

[47] Bange J P *et al* 2023 Probing correlations in the exciton landscape of a moiré heterostructure (arXiv:2303.17886 [cond-mat.mtrl-sci])

[48] Wang Y, Wang Z, Yao W, Liu G-B and Yu H 2017 Interlayer coupling in commensurate and incommensurate bilayer structures of transition-metal dichalcogenides *Phys. Rev.* B **95** 115429

[49] Meneghini G, Brem S and Malic E 2022 Ultrafast phonon-driven charge transfer in van der Waals heterostructures *Nat. Sci.* **2** e20220014

[50] Zimmermann J E, Axt M, Mooshammer F, Nagler P, Schüller C, Korn T, Höfer U and Mette G 2021 Ultrafast charge-transfer dynamics in twisted MoS_2/WSe_2 heterostructures *ACS Nano* **15** 14725–31

[51] Kunstmann J *et al* 2018 Momentum-space indirect interlayer excitons in transition-metal dichalcogenide van der Waals heterostructures *Nat. Phys.* **14** 801–5

[52] Policht V R *et al* 2023 Time-domain observation of interlayer exciton formation and thermalization in a $MoSe_2$/WSe_2 heterostructure (arXiv:2304.03707 [cond-mat.mtrl-sci])

[53] Alexeev E M *et al* 2019 Resonantly hybridized excitons in moiré superlattices in van der Waals heterostructures *Nature* **567** 81–86

[54] Tran K *et al* 2019 Evidence for moiré excitons in van der Waals heterostructures *Nature* **567** 71–75

[55] Seyler K L, Rivera P, Yu H, Wilson N P, Ray E L, Mandrus D G, Yan J, Yao W and Xu X 2019 Signatures of moiré-trapped valley excitons in $MoSe_2$/WSe_2 heterobilayers *Nature* **567** 66–70

[56] Jin C *et al* 2019 Observation of moiré excitons in WSe_2/WS_2 heterostructure superlattices *Nature* **567** 76–80

[57] Lindlau J *et al* 2018 The role of momentum-dark excitons in the elementary optical response of bilayer WSe_2 *Nat. Commun.* **9** 2586

[58] Berghäuser G, Steinleitner P, Merkl P, Huber R, Knorr A and Malic E 2018 Mapping of the dark exciton landscape in transition metal dichalcogenides *Phys. Rev.* B **98** 020301

[59] Tagarelli F *et al* 2023 Electrical control of hybrid exciton transport in a van der Waals heterostructure *Nat. Photon.* (https://doi.org/10.1038/s41566-023-01198-w)

[60] Brem S, Lin K-Q, Gillen R, Bauer J M, Maultzsch J, Lupton J M and Malic E 2020 Hybridized intervalley moiré excitons and flat bands in twisted WSe_2 bilayers *Nanoscale* **12** 11088–94

[61] Brem S, Selig M, Berghaeuser G and Malic E 2018 Exciton relaxation cascade in two-dimensional transition metal dichalcogenides *Sci. Rep.* **8** 8238

[62] Karni O *et al* 2019 Infrared Interlayer Exciton Emission in MoS_2/WSe_2 Heterostructures *Phys. Rev. Lett.* **123** 247402

[63] Zhu H, Wang J, Gong Z, Kim Y D, Hone J and Zhu X Y 2017 Interfacial charge transfer circumventing momentum mismatch at two-dimensional van der Waals heterojunctions *Nano Lett.* **17** 3591–8

[64] Li Y, Chernikov A, Zhang X, Rigosi A, Hill H M, van der Zande A M, Chenet D A, Shih E-M, Hone J and Heinz T F 2014 Measurement of the optical dielectric function of monolayer transition-metal dichalcogenides: MoS_2, $MoSe_2$, WS_2 and WSe_2 *Phys. Rev.* B **90** 205422

[65] Karni O *et al* 2022 Structure of the moiré exciton captured by imaging its electron and hole *Nature* **603** 247–52

[66] Taniguchi T and Watanabe K 2007 Synthesis of high-purity boron nitride single crystals under high pressure by using Ba–BN solvent *J. Cryst. Growth* **303** 525–9

[67] Ulstrup Søren, Koch R J, Schwarz D, McCreary K M, Jonker B T, Singh S, Bostwick A, Rotenberg E, Jozwiak C and Katoch J 2019 Imaging microscopic electronic contrasts at the interface of single-layer WS_2 with oxide and boron nitride substrates *Appl. Phys. Lett.* **114** 151601

[68] Keunecke M *et al* 2020b Electromagnetic dressing of the electron energy spectrum of Au(111) at high momenta *Phys. Rev.* B **102** 161403

[69] Li A *et al* 2022 Multidimensional multiphoton momentum microscopy of the anisotropic Ag(110) surface *Phys. Rev.* B **105** 075105

[70] Düvel M *et al* 2022 Far-from-equilibrium electron–phonon interactions in optically excited graphene *Nano Lett.* **22** 4897–904

[71] Jansen G S M *et al* 2020 Efficient orbital imaging based on ultrafast momentum microscopy and sparsity-driven phase retrieval *New J. Phys.* **22** 063012

[72] Schmitt D *et al* 2023 Ultrafast nano-imaging of dark excitons (arXiv:2305.18908 [cond-mat.mes-hall])

[73] Wilson N R *et al* 2017 Determination of band offsets, hybridization and exciton binding in 2D semiconductor heterostructures *Sci. Adv.* **3** e1601832

[74] Stansbury C H *et al* 2021 Visualizing electron localization of WS_2/WSe_2 moiré superlattices in momentum space *Sci. Adv.* **7** eabf4387

[75] Jones A J H *et al* 2021 Visualizing band structure hybridization and superlattice effects in twisted MoS_2/WS_2 heterobilayers *2D Mater.* **9** 015032

[76] Weinelt M, Kutschera M, Fauster T and Rohlfing M 2004 Dynamics of exciton formation at the Si(100) $c(4 \times 2)$ surface *Phys. Rev. Lett.* **92** 126801

[77] Zhu X Y 2014 How to draw energy level diagrams in excitonic solar cells *J. Phys. Chem. Lett.* **5** 2283–8

[78] Perfetto E, Sangalli D, Marini A and Stefanucci G 2016 First-principles approach to excitons in time-resolved and angle-resolved photoemission spectra *Phys. Rev.* B **94** 245303

[79] Rustagi A and Kemper A F 2018 Photoemission signature of excitons *Phys. Rev.* B **97** 235310

[80] Christiansen D, Selig M, Malic E, Ernstorfer R and Knorr A 2019 Theory of exciton dynamics in time-resolved ARPES: intra- and intervalley scattering in two-dimensional semiconductors *Phys. Rev.* B **100** 205401

[81] Tanimura H, Tanimura K and van Loosdrecht P H M 2019 Dynamics of incoherent exciton formation in Cu_2O: time- and angle-resolved photoemission spectroscopy *Phys. Rev.* B **100** 115204

[82] Man M K L *et al* 2021 Experimental measurement of the intrinsic excitonic wave function *Sci. Adv.* **7** eabg0192

[83] Bennecke W *et al* 2023 Multiorbital exciton formation in an organic semiconductor (arXiv:2303.13904 [cond-mat.mes-hall])

[84] Steinhoff A, Florian M, Rösner M, Schönhoff G, Wehling T O and Jahnke F 2017 Exciton fission in monolayer transition metal dichalcogenide semiconductors *Nat. Commun.* **8** 1166

[85] Merkl P *et al* 2020 Twist-tailoring coulomb correlations in van der Waals homobilayers *Nat. Commun.* **11** 2167

[86] van der Zande A M *et al* 2014 Tailoring the electronic structure in bilayer molybdenum disulfide via interlayer twist *Nano Lett.* **14** 3869–75

[87] Liu K, Zhang L, Cao T, Jin C, Qiu D, Zhou Q, Zettl A, Yang P, Louie S G and Wang F 2014 Evolution of interlayer coupling in twisted molybdenum disulfide bilayers *Nat. Commun.* **5** 4966

[88] Jin Z, Li X, Mullen J T and Kim K W 2014 Intrinsic transport properties of electrons and holes in monolayer transition-metal dichalcogenides *Phys. Rev.* B **90** 045422

[89] Cui Q, Ceballos F, Kumar N and Zhao H 2014 Transient absorption microscopy of monolayer and bulk WSe_2 *ACS Nano* **8** 2970–6

[90] Trovatello C *et al* 2020 The ultrafast onset of exciton formation in 2D semiconductors *Nat. Commun.* **11** 5277

[91] Yuan L, Zheng B, Kunstmann J, Brumme T, Kuc A B, Ma C, Deng S, Blach D, Pan A and Huang L 2020 Twist-angle-dependent interlayer exciton diffusion in WS_2–WSe_2 heterobilayers *Nat. Mater.* **19** 617–23